

EXPERIMENTAL AND NUMERICAL INVESTIGATIONS ON INTEGRATED INTAKES FOR AGILE AND HIGHLY SWEEPED AIRCRAFT CONFIGURATIONS

S. Koch, M. Rütten, and M. Rein
DLR, Institute for Aerodynamics and Flow Technology
Bunsenstrasse 10, 37073 Göttingen, Germany

Abstract

An experimental study on the effect of boundary layer ingestion into highly integrated intakes is reviewed. First, a generic intake model that has been specially designed for the tests is introduced. Thereafter, the experimental approach that allows for independently varying Mach and Reynolds number as well as boundary layer thickness and mass flux through the intake, is described. The experiments were performed in the Cryogenic Ludwig-Tube Göttingen of the German Dutch Wind Tunnels (DNW-KRG). Intake performance is discussed in terms of circumferential distortions and total pressure-recovery at the engine face. In a subsequent numerical study efficiencies of vortex generators are evaluated as a means for improving conditions at the engine face.

1. INTRODUCTION

Air intakes for jet engines of agile and highly swept aircraft configurations are usually integrated into the fuselage or wings. Typically this is connected with non-circular inlets and curved diffusers. Furthermore, due to the installation of the intake close to the wetted surface of the aircraft boundary layers formed ahead of the intake need to be considered. Usually boundary layers are diverted but there is evidence that the ingestion of boundary layers may actually increase the efficiency of the engine^{[1],[5]}. The effect of the ingestion of a boundary layer into high aspect ratio intakes with S-shaped diffusers has been the topic of an experimental study at the Institute of Aerodynamics and Flow Technology of the German Aerospace Center, DLR. The current paper reviews results of this study. Details can be found elsewhere^{[6],[7]}. In addition, a preliminary numerical investigation into the effect of vortex generators on flow conditions at the engine face is presented. The experimental part of the investigations was embedded in the GARTEUR Aerodynamics Action Group AD/AG-46 "Highly Integrated Subsonic Air Intakes"^{[8],[9]}.

For the experimental study, a generic intake has been designed, and tested at Mach numbers $M = 0.30 - 0.65$ and Reynolds numbers per unit length of up to $Re_l = 100 \cdot 10^6 \text{m}^{-1}$ in a blow down tunnel. Main features of the intake design are as follows: The entrance to the intake is rectangular, with an aspect ratio of 1:5. In the subsequent S-shaped diffuser the cross section gradually turns into a circular form at the engine face. In order to study the effect of boundary layer ingestion, the intake is arranged on a flat plate. The boundary layer that is formed on the plate, is then ingested into the intake. At the engine face distortion and pressure recovery are determined by a total pressure rake. This experimental procedure has been used to study the effect of Mach and Reynolds number as well as that of boundary layer thickness and mass flux through the intake independently of each other.

The combination of an S-duct and the low energy fluid of the ingested boundary layer typically leads to flow separation within the diffuser and thus to a highly distorted pressure distribution and losses in total pressure at the engine face. These consequences can be mitigated by applying measures of flow control within the diffuser, for example, see^{[10],[11]}. Investigations of the effectiveness of devices of flow control, particularly of vortex generators, are the topic of an upcoming experimental study. In order to prepare for the upcoming experiments, a numerical study has been started in which design and effective placement of vortex generators are investigated. In particular, the effect of pairs of vortex generators has been considered. For constant flow conditions characteristic flow structures of the uncontrolled and controlled case are compared with each other. Another topic addressed in the numerical study concerns the ingestion of a vortex into the intake. This is considered in the context of intakes that are arranged on the upper surface of wings of highly swept aircraft configurations. Maneuvers can lead to the occurrence of additional leading edge vortices or to a displacement of existing vortices that subsequently become ingested into the intake. The resulting changes in distortions are also subject of the upcoming experimental study.

2. EXPERIMENTAL SETUP AND PROCEDURE

2.1. Intake Model

The intake has been designed analytically. At the throat it is nearly rectangular with an aspect ratio of 1:5. The cross sectional shape then changes gradually into a circular shape at the location of the engine face. This location is chosen as the aerodynamic interface plane (AIP), see Figure 1. At the AIP the distribution of the total pressure is determined by a distortion rake (see section 2.2). In the diffuser following behind the throat the area distribution is linear. Ahead of the throat an ellipsoidal lip profile is added. The internal lip profile that connects the cross sections at the throat and the capture area is defined as a quarter-

ellipse. Its external profile is based on a NACA-1 profile^[12]. From the throat to the AIP the axis of the duct is displaced in the vertical direction resulting in an S-shaped course. The size of the capture area is $A_c = 133.1\text{mm} \times 28.4\text{mm}$ and at the engine face the diameter of the intake equals $2r_f = 70\text{mm}$. For details, see Rein *et al.*^[13].

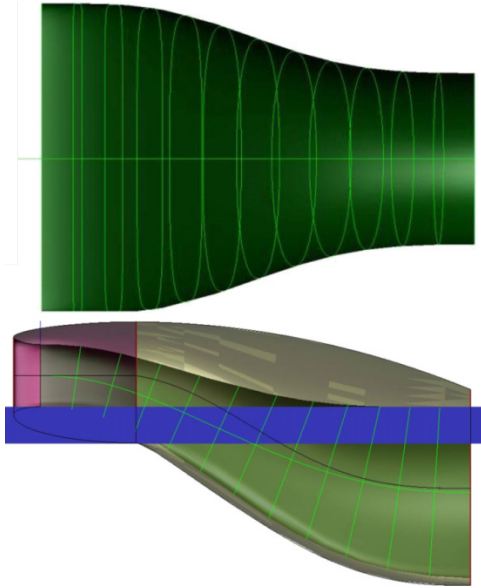


Figure 1: Contour of the generic intake (green) with lip profile and cowling (purple and grey/brown), and plate (blue): top and side view.

After the location of the engine face, the intake duct is extended by an exhaust duct of constant cross sectional area. The duct extends downwards over the length of the plate with its open end being located at the end of the test section, see Figure 2.

For the tests in the DNW-KRG the intake has been mounted on a flat plate. The leading edge of the plate is of elliptical shape. Near the leading edge the boundary layer is tripped by transition dots. Plates of three different lengths have been used ahead of the capture area, see Figure 2.

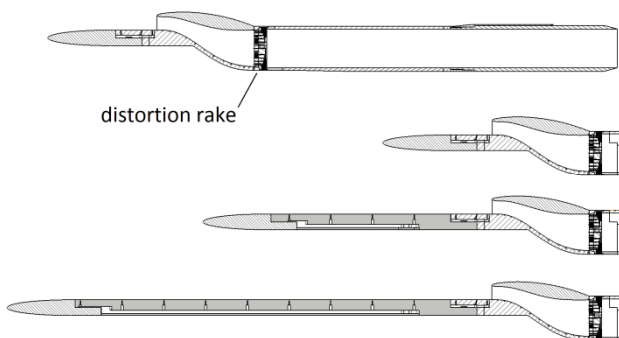


Figure 2: Side view of intake mounted on plates of various lengths, and exhaust duct (the rake is also sketched). Top: intake with short plate ($l_c = 0.209\text{m}$) and exhaust duct. Lower three drawings: intake with short, middle ($l_c = 0.554\text{m}$) and long plate ($l_c = 0.929\text{m}$) (exhaust duct truncated).

2.2. Measurement Techniques

All tests were performed in the cryogenic blow-down tunnel DNW-KRG of the German Dutch Wind Tunnels. The DNW-KRG is based on the Ludwig-tube concept^{[14]-[16]}. It can be operated at stagnation pressures up to 1MPa and charge temperatures down to about 120K. In this manner Reynolds numbers per unit length, Re_l , of up to about $4 \cdot 10^8\text{m}^{-1}$ can be achieved. Test times of the DNW-KRG lie between 0.6s and 1.0s.

In all tests the adaptive test section of the DNW-KRG was used. This section has a width of 400mm, a height of 350mm and a length of 2000mm. In the present case the model consisting of intake, plate and exhaust duct is relatively large and can cause a blockage. This poses a limit to the maximum free-stream Mach number. In the present tests Mach numbers were varied between $M = 0.30$ and $M = 0.65$.

The adaptive walls have not only been used to diminish blockage effects of the plate with intake and cowling but also for changing the pressure at the end of the test section where the exit of the exhaust pipe following after the AIP is located. In this manner the pressure gradient between capture area of the intake and exit of the exhaust pipe can be regulated. This procedure is used to adjust the mass flux through the intake.

At the AIP the distribution of the total pressure is determined by a newly designed and built distortion rake. The cross sectional area of the AIP is rather small. In order to compensate for the space taken up by the rake the cross sectional area of the intake is enlarged at the location of the rake. In addition, the rake has been equipped with only six arms. The arms can be rotated in a circumferential direction. In succeeding runs pressures are determined with the arms being located in different circumferential positions at otherwise same test conditions. In this manner the resolution of the pressure field is increased. A sketch of the rake is displayed in Figure 3.

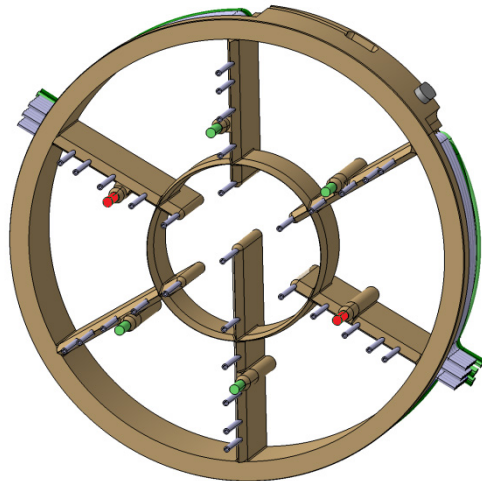


Figure 3: Rotatable distortion rake (orientation: $\varphi = 0^\circ$) with 31 Pitot pressure tubes (grey), piezoelectric pressure transducers (green) and thermocouples (red).

One arm that extends to the centre of the AIP carries 6 Pitot tubes (one in the centre), the other arms 5 Pitot tubes each. In addition, 4 Kulite pressure transducers and 2 temperature sensors have been added. The orientation

of the arms is specified in terms of the azimuthal angle φ between the extended arm and the 6 o'clock position.

For forming the distortion coefficient the mean velocity at the AIP needs to be determined. It is calculated using total pressures obtained at the rake and values of the static pressure that are obtained at 15 pressure taps distributed circumferentially in the wall of the intake, at a location just ahead of the mouths of the Pitot pressure tubes on the rake^[6].

Mean values of all quantities are obtained by sampling logged data over a time window of 0.1s that is located at the end of the test time. In this manner the influence of slight variations of free stream flow conditions that cannot be totally avoided during a particular run, is minimized.

2.3. Evaluation of Data

The boundary layer thickness, and thus the boundary layer capture ratio, depends on the particular flow conditions in the shock tunnel. In the present case of a rectangular entry area, the boundary layer capture ratio can directly be expressed by the ratio δ/h between the boundary layer thickness δ and the height h of the capture area ($h = 28.4\text{mm}$). Under typical experimental conditions boundary layer capture ratios are $\delta/h \approx 0.10 - 0.39$. In this, the boundary layer thickness has been approximated by the classical formula for incompressible turbulent boundary layers on a plate. In the case of the longest plate where the boundary layer thickness is greatest, this approximation has been checked by using a boundary layer rake that was located on the plate near the intake. At a Mach number of $M = 0.6$ where the flow is fully compressible, the agreement between incompressible flow theory and measured data is surprisingly good. With plate lengths available in the present study the influence on the boundary layer capture ratio of the plate was much greater than that of the Reynolds number. Therefore, in the following the importance of the boundary capture ratio is often indirectly considered by only stating the length of the plate.

The non-dimensional mass flux through the ducts is expressed in terms of inverse flow ratios $\mu = A_c / A_\infty$, where A_c denotes the capture area, i.e., of the cross sectional area at the entrance of the intake, and A_∞ the cross sectional area of the stream tube that is captured by the intake. The inverse flow ratio is calculated based on the mass flux densities in the AIP, θ_{AIP} , and in the free stream, θ_∞ ^[17].

The circumferential distortion coefficient, DC60, is defined following Seddon and Goldsmith^[18],

$$(1) \quad DC60 = \frac{\max(\overline{p_{0,AIP}} - \overline{p_{0,60^\circ}})}{\overline{q_{AIP}}},$$

where $\overline{p_{0,AIP}}$ is the mean total pressure in the AIP, $\overline{p_{0,60^\circ}}$ the mean total pressure in a sector of 60° degrees, and $\overline{q_{AIP}}$ is the mean dynamic pressure in the AIP. The latter is a function of the mean total and static pressure. When the mean total pressure in the AIP is considered on its own it is scaled by the free-stream value of the total pressure: $\overline{p_{0,AIP}}/p_{0,\infty}$.

Distributions of the total pressure in the AIP are determined from pressure data measured at the Pitot tubes on the rake by a Kriging interpolation method^[19]. In this, all pressure values that have been obtained in succeeding runs with different rake orientations but at same test conditions are used. In this manner the spatial resolution of the

measurements is increased. In a series of pre-tests the number of rake orientations that is needed to obtain satisfactory values of the distortion coefficient has been determined. This is described in the following paragraphs.

In the pre-tests, runs have been performed with rake orientations of $\varphi = 0^\circ$, $\varphi = 30^\circ$ and $\varphi = 15^\circ$. With the former two orientations Pitot tubes are arranged symmetrically with respect to the symmetry plane of the model. When $\varphi = 15^\circ$ this is no longer the case. Therefore, results for $\varphi = 15^\circ$ are symmetrized. This is accomplished by using $\varphi = 15^\circ$ values also at a virtual $\varphi = -15^\circ$ orientation. In doing so values of $\varphi = 15^\circ$ are simply mirrored at the symmetry plane. In this, it is assumed that the flow is symmetric with respect to the symmetry plane. In Figure 4 pressure distributions obtained in this manner with one or several orientations of the rake are compared with one another. In detail, the following configurations are compared, ordered according to the number, n , of Pitot pressures considered: $\varphi = 0^\circ$ ($n = 31$), $\varphi = 0^\circ/30^\circ$ ($n = 61$), $\varphi = 0^\circ/15^\circ/15^\circ \rightarrow -15^\circ$ ($n = 91$), and $\varphi = 0^\circ/30^\circ/15^\circ/15^\circ \rightarrow -15^\circ$ ($n = 121$).

The comparison of Figure 4 shows that pressure distributions obtained with more than one rake orientation/run look quite similar, although subtle differences are visible, particularly at the apex where the lateral extend of the low pressure region increases with the number of Pitot tubes considered. Locations of corresponding pressure tubes are indicated by black dots. Note, that one Pitot tube was flawed. The corresponding location is not marked by a black dot.

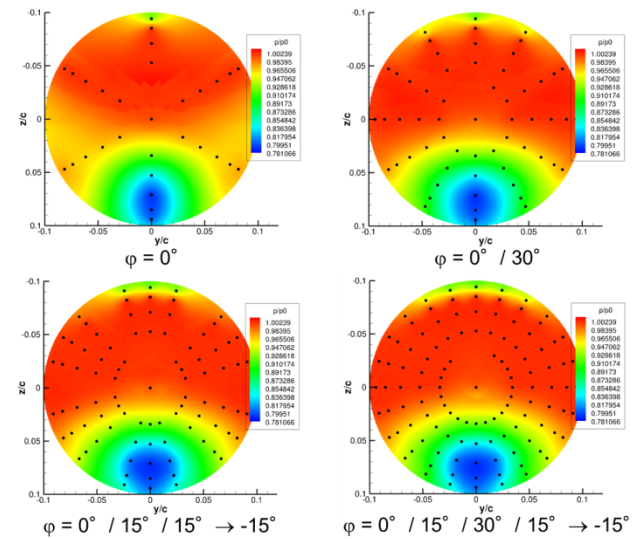


Figure 4: Comparison of distributions of the total pressure in the AIP reconstructed from pressure data obtained with different orientations of the distortion rake for $M = 0.60$, $Re_1 = 30 \cdot 10^6 \text{m}^{-1}$ and a short plate ahead of the intake. Rake orientations are provided in the figure.

Next, distortion coefficients calculated based on pressure distributions obtained with different rake orientations as shown in Figure 4 are presented in Figure 5 for a Mach number range of $M = 0.40 - 0.65$. As can be seen, with only one rake position ($\varphi = 0^\circ$) the distortion coefficient becomes strongly underestimated. In contrast, results relating to the two approaches with the greatest number of Pitot pressures ($\varphi = 0^\circ/15^\circ/15^\circ \rightarrow -15^\circ$ and $\varphi = 0^\circ/30^\circ/15^\circ/15^\circ \rightarrow -15^\circ$) are quite similar. The former approach, obtained with two runs, yields slightly worse

(i.e., greater) DC60 values. The latter approach that uses results of three runs is more expansive. Therefore, hereafter pressure distributions and distortion coefficients are always determined by using data of two runs performed with two rake orientations under otherwise same conditions.

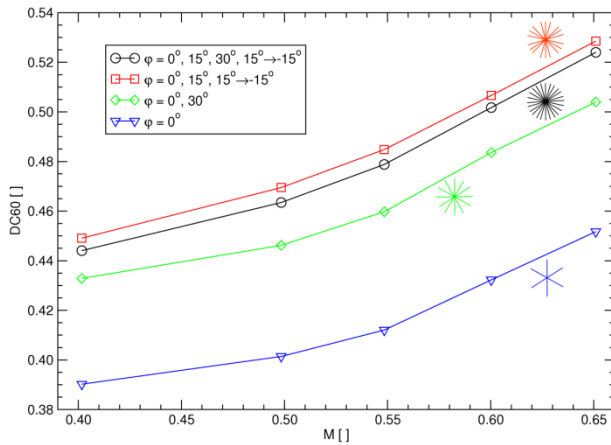


Figure 5: Dependence of the distortion coefficient on the number and type of rake orientations (see legend) considered. The dependence on the Mach number is shown at $Re_1 = 30 \cdot 10^6 m^{-1}$ and for a configuration with a short plate ahead of the intake.

3. EFFECT OF FLOW PARAMETERS ON CONDITIONS AT THE AIP

In this section the dependence of conditions at the AIP on the Mach and Reynolds number, the boundary layer capture ratio and the inverse flow ratio is presented. The conclusions are based on results of wind tunnel tests performed with parameters covering mainly the following ranges: $0.30 \leq M \leq 0.65$, $30 \cdot 10^6 m^{-1} \leq Re_1 \leq 70 \cdot 10^6 m^{-1}$, $0.10 \leq \delta/h \leq 0.39$ and $0.80 \leq \mu \leq 1.10$. In order to determine the impact of a particular parameter, parameters have been varied independently of each other, i.e., one parameter was varied with the other ones fixed. Note that in the following the Reynolds number is specified as Reynolds number per unit length, Re_1 , also called a unit Reynolds number.

3.1. Boundary Layer Capture Ratio, Mach and Reynolds Number

The boundary layer capture ratio depends both on the Reynolds number and the length of the plate. Since its dependence on the Reynolds number is much weaker than that on the plate length the boundary layer capture ratio has been varied by exchanging the plates ahead of the intake at fixed values of the Reynolds number. The effect of the boundary layer capture ratio will now be considered together with the effect of the Mach number. The effect of the Reynolds number is discussed thereafter.

To begin with, in Figure 6 distributions of the total pressure at the AIP are shown for three different plate lengths and two Mach numbers. In this manner the effect of both, boundary layer capture ratio and Mach number is demonstrated. In all examples shown the inverse flow ratio has been chosen to be close to one ($\mu \approx 0.97$) and the Reynolds number is given by $Re_1 = 30 \cdot 10^6 m^{-1}$. A distinct region of reduced total pressures always appears in the lower part of the AIP. This is a manifestation of flow separation

at the lower bend of the S-shaped diffuser. Both with increasing boundary layer thickness (plate length) and Mach number the extent of this low pressure region becomes greater. For the smaller Mach number considered in Figure 6 ($M = 0.50$) the growth with boundary layer thickness is moderate. However, at the highest Mach number tested ($M = 0.65$) changes with the boundary layer thickness become quite pronounced.

The increase of the extent of the low pressure region with the boundary layer capture ratio shows that the ingestion of a boundary layer enhances the effect of flow separation that occurs at the bend of the S-shaped diffuser. In this, the transition from the high aspect ratio of the rectangular highlight area to the circular shape of the AIP may be the reason for a peculiar concentration of the low pressure in a region that is mostly well confined in azimuthal direction.

At the greater Mach number a second region of low total pressures is clearly visible at the apex of the AIP. In this example the inverse flow ratio is slightly below one ($\mu \approx 0.97$). Hence, streamlines entering the intake are contracting ahead of the highlight area and the flow becomes accelerated. After the throat this is followed by a deceleration that is connected with a positive pressure gradient. The flow thus becomes prone to separation also at the upper surface of the diffuser. These effects are more pronounced at higher Mach numbers where the area effect becomes more important.

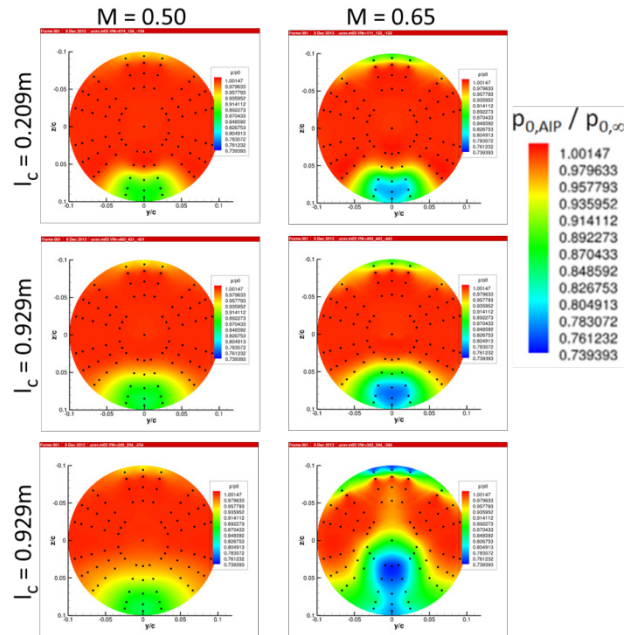


Figure 6: Effect of an ingested boundary layer and of the Mach number on the distribution of the total pressure at the AIP ($\mu \approx 0.97$, $Re_1 = 30 \cdot 10^6 m^{-1}$). Left column: $M = 0.50$, right column: $M = 0.65$. Top to bottom: boundary layer capture ratio $\delta/h \approx 0.12, 0.26$ and 0.39 (plate length: $l_c = 0.209m, 0.554m$ and $0.929m$).

The pressure distributions of Figure 6 clearly reveal that an ingestion of boundary layers and an increase of Mach numbers cause a degradation of the performance of the intake. In Figure 7, corresponding circumferential distortion coefficients, DC60, and non-dimensional mean total pressures, $\overline{p_{0,AIP}}/p_{0,\infty}$, at the AIP are considered as a quantitative measure of the performance. On the left side of Figure 7 the distortion coefficient is plotted versus the

Mach number for different Reynolds numbers and plate lengths, i.e., for different boundary layer capture ratios. The inverse flow ratio is kept constant at a value of $\mu \approx 1.04$. On the right side of Figure 7 the DC60 value is considered as a function of the mean total pressure in the AIP. The correspondence between mean total pressure and Mach number is obtained as indicated in the figure by red lines. As can be seen, for a particular combination of Reynolds number and boundary layer thickness (in Figure 7 different combinations are indicated by different curves) both, DC60 values and total pressure losses increase with the Mach number, i.e., the performance of the intake deteriorates.

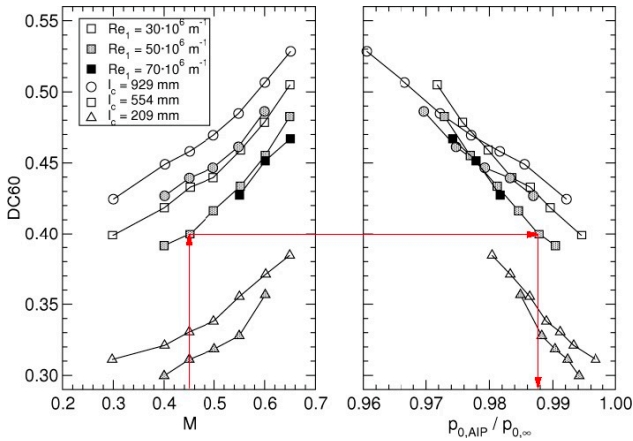


Figure 7: DC60 value as a function of the Mach number and as a function of the total pressure in the AIP for different unit Reynolds numbers and plate lengths ($\mu \approx 1.04$).

In Figure 7 a comparison of the various curves relating to different Reynolds numbers and plate lengths shows that the length of the plate affects the performance of the intake much stronger than does the Reynolds number. This reflects the different dependencies of the boundary layer thickness on these two parameters with the plate length being clearly more important (see section 2.3).

The unit Reynolds number may not only affect the boundary layer thickness but also flow separation in the diffuser. Its relatively weak effect on the intake's performance is directly obvious from the representation in Figure 8.

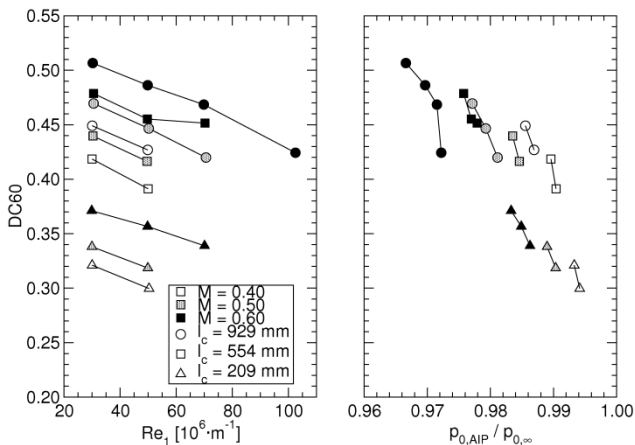


Figure 8: DC60 value as a function of the unit Reynolds number and as a function of the total pressure in the AIP for different Mach numbers and plate lengths ($\mu \approx 1.04$).

The non-dimensional mass flux is the same as in Figure 7 ($\mu \approx 1.04$). In Figure 8, different curves are related to different Mach numbers and, again, to different plate lengths. In this presentation it is directly discernible that the effect of the unit Reynolds number is much smaller than that of plate length and Mach number.

3.2. Mass Flux / Inverse Flow Ratio

The mass flux is particularly important for the performance of intakes. The effect of different mass fluxes is presented by considering the non-dimensional inverse flow ratio μ . Note that the mass flux through the intake increases with decreasing inverse flow ratio.

In Figure 9 the effect of the inverse flow ratio on the performance of a boundary layer ingesting S-duct intake is demonstrated. Distributions of the mean total pressure in the AIP are shown for two inverse flow ratios, one being less than one, the other greater than one (left and right column). Furthermore, in the upper row the boundary layer thickness entering the intake is thin, in the lower row it is thick. Mach and Reynolds number are constant, at $M = 0.6$ and $Re_1 = 30 \cdot 10^6 \text{ m}^{-1}$.

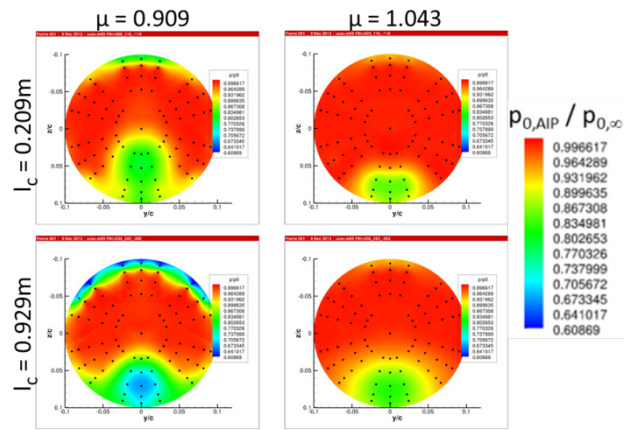


Figure 9: Effect of an ingested boundary layer and the mass flux on the distribution of the total pressure at the AIP (Mach number $M = 0.6$, $Re_1 = 30 \cdot 10^6 \text{ m}^{-1}$). Left column: $\mu \approx 0.91$, right column: $\mu \approx 1.04$; top row: $\delta/h \approx 0.12$ ($l_c = 0.209 \text{ m}$), bottom row: $\delta/h \approx 0.39$ ($l_c = 0.929 \text{ m}$).

Features observable in the pressure distributions of Figure 9 are similar to those of Figure 6. In all cases a distinct region of reduced total pressures is present in the lower part of the AIP. Its extent increases with increasing mass flux (decreasing μ) and increasing boundary layer thickness. In addition, for $\mu < 1$ a second low pressure region is formed at the apex. As already mentioned in the last section, streamlines entering the intake are contracting ahead of the intake when $\mu < 1$. If the contraction is strong, separation may occur directly at the lip of the intake. As explained before, when the Mach number is not too small flow separation can also be caused by a positive pressure gradient within the diffuser at the upper wall of the intake.

Considering the low pressure region at the apex of the AIP it is striking that this region increases strongly in circumferential direction when the boundary layer capture ratio is increased without changing the inverse flow ratio. This effect that has already been shown for an inverse flow ratio close to one ($\mu = 0.97$, see Figure 6) becomes more enhanced under the present conditions. In the preceding section the low pressure region at the apex has been

traced to an effect connected with a contraction of streamlines ahead of the intake when $\mu < 1$. Here, with increasing thickness of the boundary layer also the displacement by the boundary layer increases. Effectively, this results in a decrease of the highlight area. When the inverse flow ratio is formed with a value of the highlight area that is reduced by the effect of the displacement thickness the effective inverse flow ratio becomes smaller and thus the contraction of streamlines intensified. Hence, the low pressure region at the apex of the AIP is affected in a similar way by the inverse flow ratio and the boundary layer capture ratio.

In Figure 10 the dependence on the inverse flow ratio of the distortion coefficient and the mean total pressure is displayed for all plate lengths considered and three Mach numbers. The Reynolds number is taken constant, again at $Re_1 = 30 \cdot 10^6 \text{ m}^{-1}$. A remarkable feature is the non-monotonic dependence of the DC60 values on μ . At a critical value of the inverse flow ratio the distortion coefficient assumes a minimum, i.e., distortions become least severe. The critical value of μ depends on both the Mach number and the boundary layer capture ratio (plate length). With decreasing Mach number and thickness of the ingested boundary layer the value of the critical mass flux through the intake at which distortions become minimal, increases.

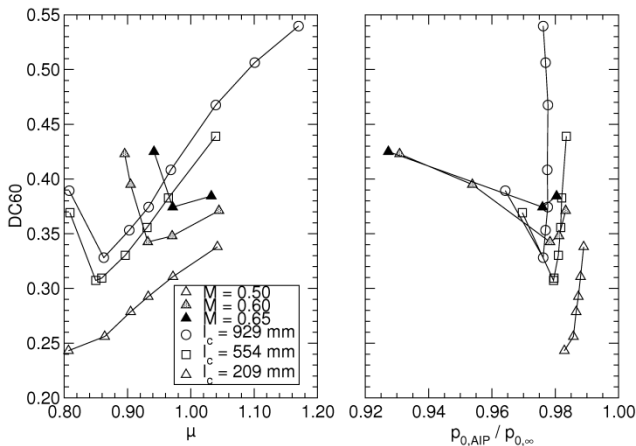


Figure 10: DC60 value as a function of the inverse flow ratio μ and as a function of the total pressure in the AIP for different Mach numbers and plate lengths ($Re_1 = 30 \cdot 10^6 \text{ m}^{-1}$).

The critical mass flux corresponding with the minimum of the distortion coefficient also plays an important role for the mean total pressure at the AIP. A comparison of the left and right graph of Figure 10 clearly shows that above the critical value of μ the non-dimensional mean total pressure and thus the loss in total pressure is nearly independent of the inverse flow ratio. However, below the critical value the mean total pressure decreases strongly, i.e., pressure losses increase with the mass flux through the intake.

The onset of the decrease of the mean total pressure is connected with the appearance of a low pressure region at the apex of the AIP (see, for example, pressure distributions in Figure 6 and Figure 9). As soon as the mass flux is increased beyond a threshold that leads to boundary layer separation at the upper wall of the diffuser the distortion coefficient increases and the mean total pressure begins to decrease. Concurrently, at the bottom of the AIP the region of low total pressures becomes extended in

radial direction towards the center of the AIP. It suggests itself that it is the appearance of the additional low pressure region at the apex that causes the onset of the decrease of the mean total pressure. Similarly, the coincident increase of the distortion coefficient is likely caused by the concurrent radial expansion of the low pressure region at the bottom of the AIP.

4. PRELIMINARY NUMERICAL STUDY ON THE EFFECT OF VORTEX GENERATORS

4.1. Application of Vortex Generators

The experimental study reported in the preceding sections will be continued in two directions. The first concerns the improvement of conditions at the AIP by applying measures of flow control within the diffuser. Subsequently, the effect on the pressure distribution at the AIP of ingesting a major disturbance into the intake will be considered. In each case vortex generators are used, in the first case as a device for flow control, in the second case for producing a well-developed vortex within the flow approaching the intake. The suitable dimensioning and positioning of the vortex generators is the objective of a current numerical study. The approach and first results are reported in the following.

The diffuser is S-shaped and its cross-sectional shape changes from a rectangular shape with high aspect ratio to a circular shape at the AIP. The effect of this complicated geometry on the flow in the diffuser is twofold. On the curved lower surface of the diffuser the flow is always prone to separation. Furthermore, centrifugal forces can lead to the formation of a pair of Dean vortices thus resulting in significant swirl at the AIP. In order to reduce the negative effect of both separated flows and vortical flows, a pair of vortex generators is arranged symmetrically with respect to the symmetry plane on the lower surface of the diffuser. A CAD drawing of the intake with a pair of vortex generators is shown in Figure 11. The idea behind this arrangement is to reenergize the fluid of the boundary layer and simultaneously add vorticity to the flow that counteracts that of the Dean vortices. In the numerical study the particular arrangement of the pair of vortex generators is varied and resulting efficiencies are discussed in a comparative analysis.

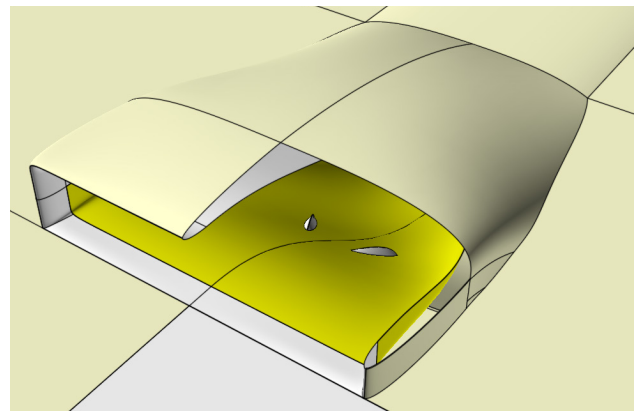


Figure 11: CAD drawing of a pair of vortex generators on the lower surface of the S-shaped diffuser

Under maneuvering flight conditions vortices formed at the leading edge of highly swept aircraft configurations can become displaced. When an integrated intake is arranged on the upper surface of a wing, this can lead to an inges-

tion of the vortical flow by the intake, subsequently causing additional inhomogeneities in the distribution of the total pressure at the AIP. This is another problem to be studied in the upcoming experimental study. In order to produce a well-defined disturbance a vortex will be formed using a vortex generator that is placed unsymmetrically with respect to the symmetry plane onto the plate ahead of the intake. The second objective of the current numerical study is the determination of suitable dimensions and positions for the vortex generator. In Figure 12 the CAD drawing of the intake configuration with a vortex generator in front is shown.

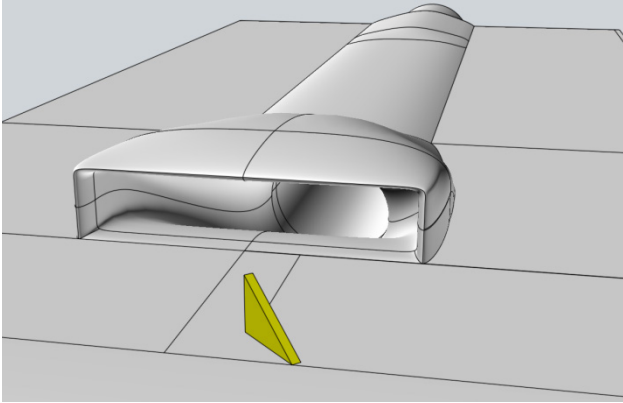


Figure 12: CAD drawing of the intake configuration with a single vortex generator element in front of the partially submerged intake.

4.2. Flow Solver and Simulation Parameters

The numerical flow investigations are performed by steady Reynolds averaged Navier-Stokes (RANS) simulations. It is well-known that flow separation, especially of vortical flows, can be highly unsteady. In the following it is assumed that unsteady effects are negligible, especially in the limited space of an intake. The calculations have been performed on a Linux cluster using the DLR compressible finite volume solver TAU^[20]. The code that allows for a second order spatial and temporal discretization, has been well validated by a variety of experimental and numerical validation campaigns and is state of the art with respect to performance, efficiency and accuracy^[21]. Modeling of turbulence, in particular for situations where flow separation occurs, is still challenging. Here, the Wilcox $k-\omega$ turbulence model with the SST extension has been applied. This model yields a good representation of the wall shear stress and has the capability to produce reasonable results also for separated flows. Different numerical acceleration techniques have been used. The flux splitting technique permits to perform inner subiterations for simulation speed up. In addition, implicit residual averaging and a 4-w multigrid cycle has been applied to further accelerate the CFD calculations.

The configuration considered is the generic intake model without and with vortex generators, mounted on the short plate. In the experiments the model is integrated in a wind tunnel. However, in order to reduce the computational efforts, the wind tunnel was omitted in the computations. The free stream Mach number has been set to $M = 0.6$, analogous to corresponding wind tunnel experiments. This results in a free stream velocity of nearly 188m/s at the intake entry plane. Similarly, the Reynolds number has been set to 29.8 million based on a length of $l = 1.0\text{m}$, as in many of the experiments. In order to achieve compara-

ble data, wind tunnel conditions have also been assumed in the computations: the temperature has been set to 246.15K and the ambient pressure to 178kPa.

In the calculations the CFL number was set to 0.8 and 10.000 iterations have been computed for each simulation run. The residual declined four orders of magnitude. For generating CFD meshes the commercial mesh generator "Centaur" from CentaurSoft has been applied. Many mesh studies have been performed, on the one hand in order to find the right meshing parameters for achieving a high grid-quality mesh that is necessary to resolve the boundary layer, on the other hand in certain regions a fine spatial resolution of the flow field is a pre-condition to correctly reproduce flow structures like vortices and flow separation.

The CFD study has been conducted on a locally pre-refined hybrid grid. It consists of nearly 26 million points and 69 million cells, 27 million tetrahedra and 42 million prismatic cells in 30 pseudo structured layers. The first initial prism layer height has been set to $4 \cdot 10^{-4}\text{m}$ and the growth rate for the prism stacks to 1.12 in the mesh generator Centaur. The high number of prism stacks is necessary to have a fine spatial resolution close to the walls and a smooth transition to the free flow. This is also essential for resolving the boundary layer and, therewith, to be able to reproduce the right location of flow separation. Also the resolution of developing vortices is possible. Preceding CFD simulations helped to adjust the y^+ value to 1 in a grid adaptation step.

4.3. Discussion of Numerical Results

This section provides a first look at the results of the numerical study. A main part of the analysis of the numerical simulations consists of describing the vortical flow structures, and of losses in total pressure and the corresponding inhomogeneous pressure distribution at the AIP. The vortical flow structures are visualized by line integral convolution (LIC) techniques using in-plane velocities at the AIP. Special attention is also given to the development of the wall shear stress along the curved intake duct/diffuser, again projected flow structures are visualized by applying LIC. An example of the results of a visualization is depicted in Figure 13.

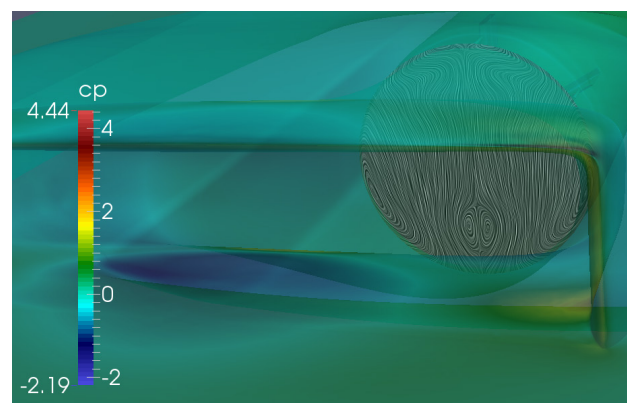


Figure 13: No flow control: Distribution of C_p values on the surface of the intake model, and visualization of the in-plane velocity structure at the AIP by using line integration convolution indicating Dean vortices. $M = 0.60$, $Re_l = 29.8 \cdot 10^6 \text{m}^{-1}$, short plate, $\mu = 0.92$.

Here, the reference case of an uncontrolled flow field is shown. The signature of Dean vortices is observable at the AIP. The corresponding results of a LIC visualization

of the wall shear stress are shown in Figure 14. On the lower surface of the intake duct, lines representing the wall shear stress converge towards an attractor point. A closer look at such indications of flow separation will be the key element in designing vortex generators.

The distortion coefficient relating to the numerical solutions is determined using a reconstruction technique that is analogous to the experimental procedure^[22]. In this, DC60 values are calculated from single values of the total pressure. The values are taken at the same locations as in the pointwise measurements with the distortion rake. The comparison of DC60 values is a major point in the analysis and evaluation of the efficiency of the applied vortex generators. Additionally, another distortion criterion ψ has been defined to evaluate the effect of flow control devices. Since the vorticity distribution of the manipulated flow field is more spread in the yz-plane in regard to the reference case, the ratio ψ of the area averaged in-plane velocity magnitude to the overall area averaged velocity magnitude can be used to quantify the flow inhomogeneity at the AIP.

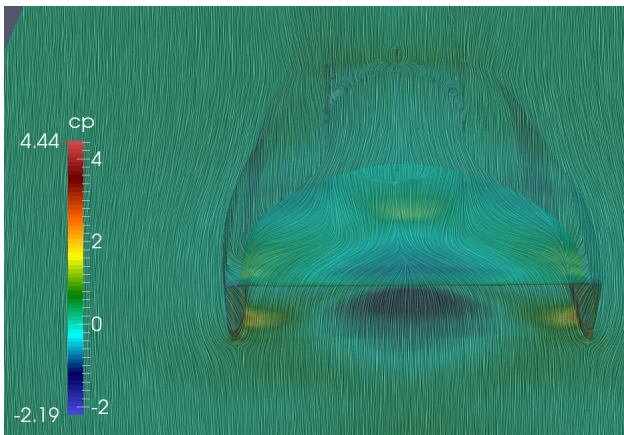


Figure 14 No flow control: Visualization by line integration convolution of the wall shear stress within the intake on the curved intake duct. Flow separation is indicated by convergent wall shear stress lines. $M = 0.60$, $Re_1 = 29.8 \cdot 10^6 \text{ m}^{-1}$, short plate, $\mu = 0.92$.

Different vortex generator configurations have been investigated in order to reduce inhomogeneities induced by Dean vortices. The topology of the generators has always been the same, however, three different heights of the vortex generator pairs have been realized. In Figure 15 comparative illustrations of the results are shown. Besides the distribution of C_p values on the surface of the intake model the visualization of the in-plane velocity structure at the AIP is shown by using line integration convolution. Additionally total pressure losses are colored coded. The vortex generators have counteracted the Dean vortices by splitting the separation line and relocating the separation outwards. Additionally they have induced other smaller counter-rotating vortices. The newly generated vortical flow structure differs in size, distance and total pressure losses. The results show that new vortex pairs are developing further downstream. Analyzing the flow structure of the in-plane velocity also reveals that the VG pair induced flow effect is too strong since new counter-rotating vortices occur. In contrast to the uncontrolled case a weak top-down flow can be observed in the middle of the vortical region, which leads to a redistribution of total pressure losses: The total pressure loss is now concentrated in two

spots. Eventually this can be beneficial in regard to the flow field homogeneity requirements at the AIP.

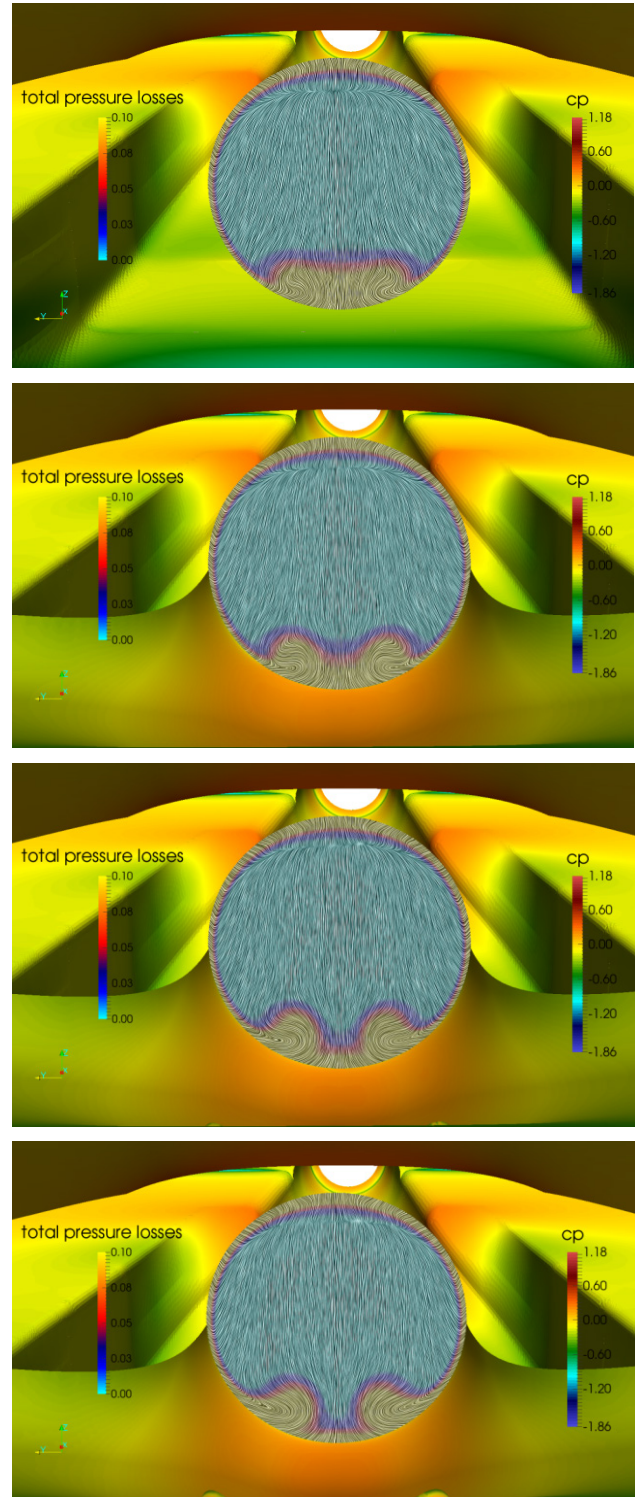


Figure 15: Flow control by pairs of vortex generators. Top: uncontrolled reference case; second from top: smallest VG pair; second from bottom: medium high VG pair; bottom: highest VG pair. C_p distribution on the surface of the intake model and visualization of the in-plane velocity structure at the AIP by using line integration convolution. At the AIP total pressure losses are color coded. $M = 0.60$, $Re_1 = 29.8 \cdot 10^6 \text{ m}^{-1}$, short plate, $\mu = 0.984$.

The LIC visualization of the wall shear in Figure 16 confirms that the vortex generator pair is able to prevent the generation of Dean vortices. Thus the proposed method is able to reduce the parasitic flow effect due to the strong curvature of the intake channel. An optimization process will be applied in order to further improve the homogeneity of the flow field at the AIP.

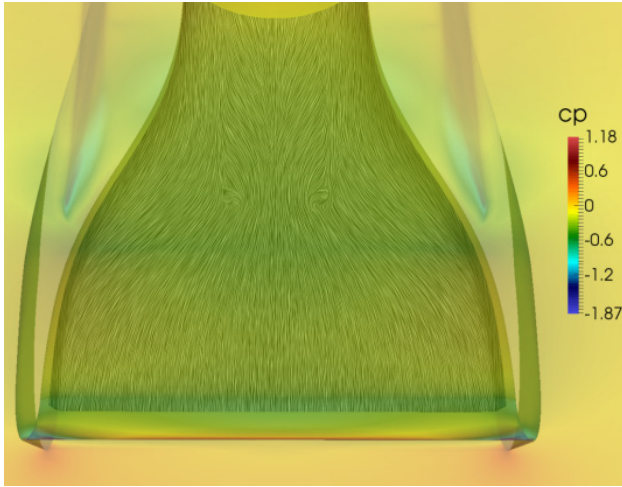


Figure 16: Flow control by pair of vortex generators: Visualization by line integration convolution of the wall shear stress within the intake on the curved intake duct. The small vortex generators have reduced flow separation by limiting the region of convergent wall shear stress lines. $M = 0.60$, $Re_1 = 29.8 \cdot 10^6 \text{ m}^{-1}$, short plate, $\mu = 0.984$.

Finally, DC60, relative total pressure and distortion values are compared for the symmetric VG pair flow cases. The results are listed in Table 1. It can be observed, that the highest VG pair shows the best result with regard to DC60 value, however, the distortion criterion ψ is greater due to a double concentration of newly generated swirling flow, which indicates that this configuration has to be further improved. One has to remark that these criteria have a limited explanatory power due to their averaging behavior, thus new criteria have to be developed in order to improve the evaluation of flow inhomogeneities at the AIP.

	DC60	$p_0/p_{0,\infty}$	ψ
ref	0.383	0.9866	0.0604
small	0.335	0.9869	0.0605
middle	0.265	0.9873	0.0667
high	0.208	0.9870	0.0735

Table 1: Comparison of DC60 values, relative total pressure and distortion criteria ψ for the uncontrolled reference case and the three symmetric vortex generators.

The impact of outer vortices which are sucked in by the intake is demonstrated in Figure 17. A sample configuration for generating an outer vortex is shown together with values of the pressure coefficient C_p , for free stream conditions relating to $M = 0.6$ and $Re_1 = 29.8 \cdot 10^6 \text{ m}^{-1}$. In the top part of Figure 17 the footprint of the vortex entering the intake can be seen in the pressure distribution. The impact of the vortex is illustrated by the 5% iso-surface of total pressure loss in the bottom part of Figure 17.

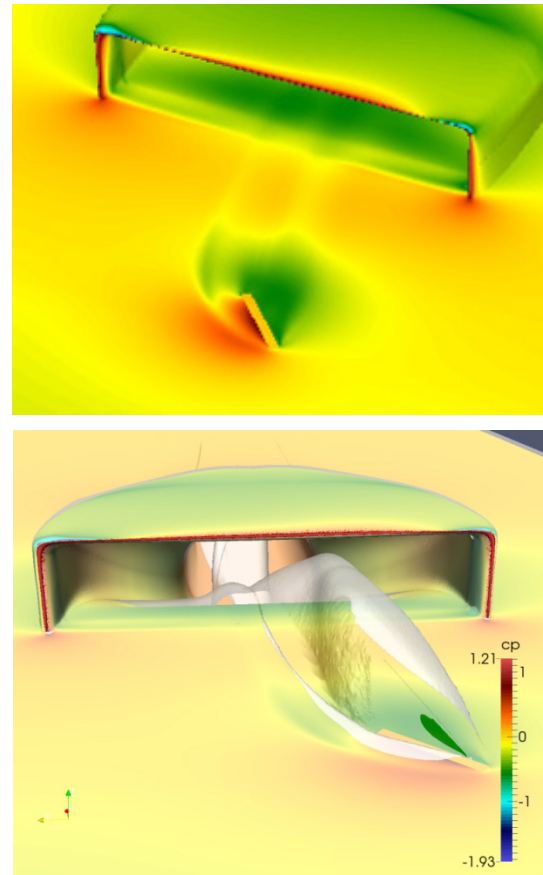


Figure 17: Impact of a vortex generator ahead of the intake on the flow: The pressure distribution (C_p) on the surface is shown for $M = 0.6$ and $Re_1 = 29.8 \cdot 10^6 \text{ m}^{-1}$. Top: view on VG in front of the intake, bottom: detailed view of vortex generator and inlet area.

5. SUMMARY

At the Institute of Aerodynamics and Flow Technology of the German Aerospace Center an experimental study has been performed on the effect of boundary layer ingestion into highly integrated intakes. The study took place against the background of requirements of agile and highly swept aircraft configurations. Due to configurational constraints the flow physics associated with intakes of such configurations is quite challenging. In addition to the occurrence of secondary flows due to curvature effects in the S-duct and changes in the cross sectional shape between entry and fan area, also the ingestion of boundary layers causes distortions and a reduced pressure recovery at the engine face. In the experimental study, not only the boundary layer capture ratio but also the Mach and Reynolds number as well as the mass flux through the intake have been varied independently of each other.

The main results of the study have been reviewed. Among other things, the displacement effect of an ingested boundary layer leads to a reduction of the effective cross sectional area of the capture area of the intake and, hence, of the effective value of the inverse flow ratio. Therefore, an increase of the boundary layer capture ratio at a constant value of the nominal inverse flow ratio and a decrease of the inverse flow ratio at a constant boundary layer capture ratio, respectively, lead to comparable changes in distribution patterns of the total pressure in the AIP. However, this does not mean that corresponding

values of the distortion coefficient are changed in the same way. As has been shown, the circumferential distortion descriptor DC60 depends non-monotonically on the inverse flow ratio. Above a critical value of the inverse flow ratio that depends both on Mach number and boundary layer capture ratio, DC60 values decrease with the inverse flow ratio, i.e., with increasing mass flux. Below the critical value of the inverse flow ratio DC60 values increase with the mass flux. In contrast, the mean total pressure at the AIP does not show a non-monotonous behavior. Above the critical value of the inverse flow ratio changes with the inverse flow ratio are negligible small. However, as soon as the mass flux is increased beyond its critical value the mean total pressure begins to decrease sharply. These behaviors have been traced to the appearance of a second regime of flow separation at the lip or upper surface of the intake when the mass flux is above its critical value. Conditions at the AIP have also been observed to deteriorate with increasing Mach number. In contrast, within the range considered Reynolds number effects were less significant than the effect of all other parameters.

So far, investigations have been carried out without applying devices for flow control for improving conditions at the AIP. This is the topic of upcoming experiments. In order to prepare for these further experimental investigations a numerical study has been started to determine suitable dimensions and positions of vortex generators to be applied within the diffuser in future tests. Furthermore, a single vortex generator placed ahead of the intake, will be used for generating a vortex that is subsequently ingested by the intake thus mimicking the effect of inhomogeneities in the free stream on the performance of the intake.

Moreover, first results of the numerical study have been presented, which demonstrate the possibility to improve the flow condition at the AIP. These very first results are promising and provide direction for further studies. The design of suitable internal vortex generators counteracting incoming vortices will be objective in upcoming optimization processes. It has also been shown that the DC60 alone is not sufficient to evaluate the flow inhomogeneity, i.e. the distortion criterion ψ reveals higher swirling ratio despite better DC60 values. Therefore, new or combinations of criteria have to be developed for the evaluation of the design of vortex generators within an optimization process.

6. REFERENCES

- [1] Betz, A., „Einführung in die Theorie der Strömungsmaschinen,” Verlag G. Braun, Karlsruhe, 1959, pp. 204ff.
- [2] Martin, P. G., „Challenges in the design of air intakes for subsonic UAVs,” *Proc. RAeS Aerospace Aerodynamics Research Conference*, June 10-12, 2003, London, 2003, pp. 23.1-6, 2003.
- [3] Plas, A. P., Sargeant, M. A., Madani, V., Chrichton, D., Greitzer, E. M., Hynes, T. P., and Hall, C. A., „Performance of a Boundary Layer Ingesting (BLI) Propulsion System,” AIAA 2007-450, 2007.
- [4] Drela, M., „Power Balance in Aerodynamic Flows,” AIAA J., Vol. 47, No. 7, 2009, pp. 1761-1771.
- [5] Arntz, A., Atinault, O., Destarac, D., and Merlen, A., „Exergy-based Aircraft Aeropropulsive Performance Assessment: CFD Application to Boundary Layer Ingestion,” AIAA 2014-2573, 2014.
- [6] Rein, M., Koch, St., and Rütten, M.; „Experimental Investigations of Ingesting Boundary Layers into a Diverterless S-Duct Intake,” AIAA 2014-0373, 2014.
- [7] Rein, M., and Koch, St.; „Experimental Study of Boundary Layer Ingestion into a Diverterless S-Duct Intake,” AIAA J. (2015), accessed September 8, 2015. doi: <http://arc.aiaa.org/doi/abs/10.2514/1.J053902>
- [8] Berens, T., Delot, A.-L., Tormalm, M., Ruiz-Calavera, L.-P., Funes-Sebastian, D.-E., Rein, M., Säterskog, M., Ceresola, N., and Zurawski, L., „Numerical and Experimental Investigations on Highly Integrated Subsonic Air Intakes,” AIAA 2014-0722, 2014.
- [9] Berens, T. M., Delot, A.-L., Tormalm, M., Ruiz-Calavera, L.-P., Funes-Sebastian, D.-E., Rein, M., Säterskog, M., and Ceresola, N., „Numerical and Experimental Investigations on Subsonic Air Intakes with Serpentine Ducts for UAV Configurations,” *Proc. 5th CEAS Air & Space Conf.*, CEAS 2015 paper no. 074, Delft, 2015 (in print).
- [10] Owens, L. R., Allan, B. G., and Gorton, S. A., „Boundary Layer Inlet Flow Control,” *J. Aircraft*, Vol. 45, No. 4, 2008, pp. 1431-1440.
- [11] Tormalm, M., „Flow Control using Vortex Generators or Micro-Jets Applied in an UCAV Intake,” AIAA 2014-0724, 2014.
- [12] Baals, D. D., Smith, N. F., and Wright, J. B., „The development and application of high-critical-speed nose inlets,” NACA Report No. 920, 1948.
- [13] Rein, M., Hannemann, M., Gardner, D. G., and Koch, S., „Design of a generic subsonic S-duct intake for studies on the effect of boundary layer ingestion,” DLR IB 224-2009 A28, DLR, 2009.
- [14] Ludwig, H., „Der Rohrwindkanal,” *Z. Flugwiss.*, Vol. 3, No. 7, 1955, pp. 206-216.
- [15] Rosemann, H., „The Cryogenic Ludwig-Tube at Göttingen,” in: *Special Course on Advances in Cryogenic Wind Tunnel Technology*, AGARD-R-812, Cologne, Germany, May 20-24, 1996.
- [16] Koch, S., „Zeitliche und räumliche Turbulenzentwicklung in einem Rohrwindkanal und deren Einfluss auf die Transition an Profilmodellen“, DLR FB-04-19, DLR, 2004.
- [17] Rein, M., and Gardner, A., „Generic lambda wing configuration in compressible flow: effect of highly integrated intakes,” *J. Aircraft* 52 (2015), pp. 972-980
- [18] Seddon, J. J., and Goldsmith, E. L., „Intake Aerodynamics”, 2nd ed., AIAA, Reston VA, 1999.
- [19] Krige, D. G., „A statistical approach to some basic mine valuation problems on the Witwatersrand,” *J. of the Chem., Metal. and Mining Soc. of South Africa*, Vol. 52, No. 6, 1951, pp. 119-139.
- [20] Gerhold, T., and Evans, J., „Efficient Computation of 3D-Flows for Complex Configurations with the DLR Tau-Code Using Automatic Adaptation,” *Notes on Numerical Fluid Mechanics*, Vol. 72, Vieweg, 1999.
- [21] Schwamborn, D., Gardner, A., von Geyr, H., Krumbein, A., Lüdeke, H., and Stürmer, A., „Development of the TAUCode for aerospace applications,” 50th NAL International Conference on Aerospace Science and Technology, 2008-06-26 - 2008-06-28, Bangalore, India, 2008.
- [22] Rütten, M., Kuckenburg, S., Koch, S., and Rein, M., „Investigation of the Flow within Partially Submerged Scoop Type Air Intakes,” AIAA 2013-2912, 2013.